1 **Structural connectivity gradient associated with a dichotomy reveals the topographic**

2 **organization of the macaque insular cortex**

3 Long Cao [1,2,+], Zongchang Du [3+], Yue Cui [2,3,4+], Yuanchao Zhang [1], Yuheng Lu [2,3,4], Baogui

4 Zhang [2,4], Yanyan Liu [2,4], Xiaoxiao Hou [2,4], Xinyi Liu [2,4], Luqi Cheng [5], Kaixin Li [6], Zhengyi

5 Yang [2,4], Lingzhong Fan [2,3,4,7,8]*, Tianzi Jiang [1,2,3,4,7,8]*

6 [1] Key Laboratory for NeuroInformation of Ministry of Education, School of Life Science and

7 Technology, University of Electronic Science and Technology of China, Chengdu 610054,

8 China

9 [2] Brainnetome Center, Institute of Automation, Chinese Academy of Sciences, Beijing 100190,

10 China

11 [3] School of Artificial Intelligence, University of Chinese Academy of Sciences, Beijing 100049,

12 China

13 [4] National Laboratory of Pattern Recognition, Institute of Automation, Chinese Academy of

14 Sciences, Beijing 100190, China

15 [5] School of Life and Environmental Sciences, Guilin University of Electronic Technology,

16 Guilin 541004, China

17 [6] School of Mechanical and Power Engineering, Harbin University of Science and Technology,

18 Harbin 150080, China

19 [7] CAS Center for Excellence in Brain Science and Intelligence Technology, Institute of

20 Automation, Chinese Academy of Sciences, Beijing 100190, China

21 [8] Research Center for Augmented Intelligence, Artificial Intelligence Research Institute,

22 Zhejiang Laboratory, Hangzhou 311100, China

23

24 + These authors contributed equally to this work.

25

26 ***Corresponding author:**

27 **Tianzi Jiang,** Brainnetome Center, Institute of Automation, Chinese Academy of Sciences,

28 Beijing 100190, China. Email: jiangtz@nlpr.ia.ac.cn

29 **Lingzhong Fan,** Brainnetome Center, Institute of Automation, Chinese Academy of Sciences,

30 Beijing 100190, China**.** Email: lingzhong.fan@ia.ac.cn

31

32 Correspondence should be addressed to Tianzi Jiang at jiangtz@nlpr.ia.ac.cn

33

Abstract

Histology studies revealed that the macaque insular cortex was characterized by the gradual organizations containing agranular, dysgranular and granular insula. However, no consensus has been reached on the elaborate subdivisions of macaque insula. Until now, no neuroimaging study to our knowledge combining connectivity-based gradients and parcellation has been performed to investigate the topographic organization of the macaque insular cortex. In this study, we used high-resolution ex vivo diffusion-weighted imaging data to explore the macaque insular cortex's global gradient organization and subdivisions. We found a rostrocaudal organization of the dominant gradient in the macaque insula using a diffusion map embedding. Meanwhile, extracting the 25% top and bottom components from the dominant and second gradient, which explained variance over 60% in total within ten gradients, the connectivity-based parcellation method was performed to subdivide each component into two subregions confirmed by the cross-validation analysis. Furthermore, permutations tests identified that two subregions from each component showed significant differences between their connectivity fingerprints. Finally, we found that the dominant and second gradients were significantly correlated with the T1w/T2w and cortical thickness maps in the macaque insula. Taken together, the global gradients combining the subdivisions examined the topographic organization of the macaque insular cortex based on the structural connectivity, which may contribute to a better understanding of the intricate insular cortex anatomy.

Keywords: Insular cortex; Rhesus monkey; Structural connectivity; Gradient; Parcellation

Abbreviations

56	6VR	area 6 of cortex, ventral part, rostral subdivision
57	8AV	area 8 of cortex, anteroventral part
58	36R	area 36, rostral part
59	Acb	accumbens nucleus
60	AK	auditory koniocortex
61	Amyg	amygdaloid nucleus
62	Gu	gustatory cortex
63	INS	insular cortex
64	IPL	Inferior parietal lobule
65	MST	medial superior temporal area
66	PaA	paraauditory area
67	PaI	parainsular cortex
68	Pd	pallidus
69	PE	parietal area PE
70	Pir	piriform cortex
71	PPt	posterior parietal area
72	ProK	prokoniocortex
73	ProM	promotor
74	ReI	retroinsular area
75	ROI	region of interest
76	S2	secondary somatosensory cortex
77	Str	striatum
78	STS	superior temporal sulcus
79	Tha	thalamus
80	TP	temporopolar area
81	TPt	temporoparietal cortex

1. Introduction

Macaque insular cortex, located in the depth of the Sylvian fissure, is structurally and functionally heterogeneous cortical region characterized by the cytoarchitectonic gradients and extensive anatomical connections with the limbic system, prefrontal, orbitofrontal, parietal and temporal lobe. Macaque insula has been demonstrated to be involved in diverse functions, such as emotions, social behavior (Caruana et al. 2011), execution (Di Cesare et al. 2019), reward (Mizuhiki et al. 2012) and also auditory (Remedios et al. 2009), gustatory (Yaxley et al. 1990), sensorimotor, orofacial motor (Jezzini et al. 2012), etc. A unique characteristic of the insula is the presence of von Economo neuron (VEN), which is associated with self-awareness and social cognition, and was originally observed only in the great ape and humans, but not other primates. However, a recent architectonic study demonstrated that the VENs also existed in the anterior insula of the macaque (Evrard et al. 2012), suggesting that the insula of macaque monkeys plays a critical role in evolutional and comparative neuroscience (Evrard 2019).

Structural organization of macaque insula is primarily obtained from cyto-, or myelo-, and receptor- architectonic studies. Using Nissl and myelin staining, Mesulam and Mufson proposed the concept of granularity and subdivided macaque insula into three architectonic areas, including argranular, dysgranular and granular insula (Ia, Id and Ig), which were just delineated by the circular sulcus and limen insulae (Mesulam and Mufson 1982). Subsequently, Carmichael and Price used multiple stains to subdivide macaque orbital and medial prefrontal cortex and found that the anterior insula subregion Ia was extended onto the posterior orbital surface and could be subdivided into five subregions, including medial, intermediate, lateral, posteromedial and posterolateral insula (Iam, Iai, Ial, Iapm and Iapl) (Carmichael and Price 1994a). Recently, using multiple immunohistochemical stains, Gallay et al. revealed that macaque insula could be into eight subregions (Ia1-2, Id1-3, Ig1-2 and G) with parallel ventral to dorsal gradients by the cytoarchitectonic features of layer II-V (Gallay et al. 2012a). After confirming the VENs in the Ia of macaque insula, Evrard et al. employed Nissl and Myelin techniques to subdivide macaque insular cortex into fifteen subregions (Evrard et al. 2014), which showed medial-lateral or ventrodorsal pattern along the rostrocaudal axis of macaque insula territory. Therefore, microstructural evidence has demonstrated that the macaque insular

111 cortex displays anterior-middle-posterior divisional patterns at a coarse level. In contrast, the

112 highly specialized subregions of macaque insula remain not well-established.

113 Following the development of neuroimaging techniques, accumulating studies have

114 focused on the organization of the human insular cortex. Initially, most neuroimaging studies

115 performed connectivity-based methods to parcellate human insula with clear boundaries.

116 However, recent neuroimaging research revealed that human insula represented global

117 gradients in macroscopic and microscopic organizations. For example, based on probabilistic

118 tractography, Cerliani et al. utilized Laplacian eigenmaps to explore the organization of human

119 insula, and unveiled the rostrocaudal gradients of structural connectivity (SC) variation across

120 the insula territory (Cerliani et al. 2012b). More recently, in one fMRI study, Tian et al. revealed

121 that human insula could be characterized as a continuum of gradual change along the

122 rostrocaudal axis and parcellated human insula into two subregions with anterior-posterior

123 pattern (Tian and Zalesky 2018). Using multi-shell diffusion-weighted imaging (DWI), Menon

124 et al. used RTOP representing granularity to investigate the microstructure of the human insular

125 cortex and found gradients along the anterior-posterior and dorsal-ventral axes (Menon et al.

126 2020). Using T1w/T2w maps, Royer et al. uncovered two principal gradients of human insula

127 myeloarchitecture showing one from ventral anterior to the posterior insula and the other from

128 dorsal anterior to both ventral anterior and posterior insula (Royer et al. 2020). Taken together,

129 apart from neuroimaging research with connectivity-based parcellation method on insula

130 organization, several studies also considered that the insular cortex was characterized with the

131 overall gradual change along the rostrocaudal or ventrodorsal axis. Until now, no neuroimaging

132 study to our knowledge used connectivity-based parcellation or gradient method or both to

133 explore the macrostructure of macaque insular cortex specifically. Therefore, the topographic

134 organization of the macaque insula, representing the connectivity variation, remains unknown.

135 In this study, we used high spatial and angular resolution ex vivo macaque DWI data to

136 investigate the topographic organization of the macaque insular cortex. First, we used a

137 diffusion map embedding to examine macaque insula global gradients. Second, extracting the

138 top and bottom components from the first two gradients, we performed connectivity-based

139 parcellation to subdivide each component to uncover the elaborated macaque insula

6

organization. Third, using connectivity fingerprints, we examined the structural connectivity differences between the subregions subdivided from one component. Finally, we explored the relationships between macaque insula global gradients and two neuroimaging indices, including T1w/T2w and thickness maps. Here, we hypothesized that the globally spatial representation of macaque insula would show a rostrocaudal gradient, and the elaborated subdivisions of macaque insula would show medial-lateral or ventrodorsal pattern along the rostrocaudal gradient.

2. Materials and methods

2.1 Data acquisition

2.1.1 Ex vivo macaque brains

Eight ex vivo macaque (*Macaca mulatta*; 2 males, 6 females; 5.6 ± 1.06 years of age) brains were collected, and the experimental protocols were approved by the National Animal Research Authority of China and the Ethics Review Committee of Biomedical Research of the Institute of Automation, Chinese Academy of Sciences. MRI data contained T2-weighted (T2w) and DWI images which were obtained from a 9.4-T horizontal animal MRI system (Bruker BioSpec 94/30 USR) with Paravision 6.0.1. The gradients were equipped with a slew rate of 4570 mT/m/ms and maximum strength of 660 mT/m. A 72 mm inner diameter quadrature radiofrequency coil achieved the radiofrequency transmission and reception. Prior to imaging, each postmortem macaque brain was soaked in 1L phosphate buffered saline with 1mM/L gadopentetate dimeglumine (Gd-DTPA) at 4 °C and shook daily for at least 1 month to reduce T1 relaxation time (D'Arceuil et al. 2007). A 3D spin-echo EPI diffusion weighted sequence was used to acquire multi-shell DWI with echo time (TE) = 25 ms, repetition time (TR) = 200 ms, 186 or 129 diffusion directions (7 brain DWI images, 6 b = 0 s/mm^2, 60 b = 1200 s/mm^2, 120 b = 4800 s/mm^2; 1 brain DWI image, 6 b = 0 s/mm^2, 30 b = 1200 s/mm^2, 93 b = 4800 s/mm^2), field of view (FOV) = $66.6 \times 54.0 \times 72.0$ mm^3, flip angle (FA) = 90°, matrix = $148 \times 120 \times 160$ and voxel size = $0.45 \times 0.45 \times 0.45$ mm^3 without gap. T2w images were obtained by a 3D MSME sequence with TE = 36 ms, TR = 2000 ms, FOV = $72.0 \times 54.0 \times 80.1$ mm^3, FA = 90°, matrix = $240 \times 180 \times 267$ and voxel size = $0.3 \times 0.3 \times 0.3$ mm^3.

169

2.1.2 In vivo macaque brains

171 Eight in vivo macaque (*Macaca mulatta*; male) brain MRI data used in this study was obtained

172 from TheVirtualBrain (Shen et al. 2019). The Animal Use Subcommittee approved the

173 experimental protocols of the University of Western Ontario Council on Animal Care. They

174 were following Canadian Council of Animal Care guidelines. The neuroimaging protocol

175 included T1-weighted (T1w) and DWI images acquired by the 7.0-T Siemens MAGNETOM

176 head scanner with a gradient (Siemens AC84 II, Gmax = 80 mT/m, SlewRate = 400 T/m/s).

177 T1w images were collected by an MP2RAGE acquisition with TR = 6500 ms, TE = 3.15 ms,

178 TI1 = 800 ms, TI2 = 2700 ms, matrix = 256×256, 128 slices and voxel size = $0.5 \times 0.5 \times 0.5$

179 mm^3, and only T1w images were analyzed in our study.

180

2.2 Data preprocessing

182 Preprocessing of macaque ex vivo DWI data included reorienting the initial brain space into

183 RAS space, denoising (Veraart et al. 2016), removing ringing artifacts (Kellner et al. 2016),

184 eddy currents correction (Graham et al. 2016), brain-tissue extraction on b0 image (Smith 2002)

185 and refining brain mask manually, which were respectively implemented in the Medical Image

186 Processing, Analysis and Visualization (MIPAV) (https://mipav.cit.nih.gov/), MRtrix3

187 (Tournier et al. 2019), FMRIB Software Library (FSL v6.0) (Woolrich et al. 2009; Jenkinson

188 et al. 2012) and ITK-SNAP (http://www.itksnap.org/). N4BiasFieldCorrection (Tustison et al.

189 2010) within Advanced Normalization Tools (ANTs) (http://stnava.github.io/ANTs/) was

190 performed to correct a b0 image for the subsequent registration. Then DTIFIT (Smith et al.

191 2004) was used to fit a diffusion model to check the principal eigenvector within brain voxels

192 in the native space. After confirming the principal eigenvector, BEDPOSTX (Jbabdi et al. 2012)

193 was performed to estimate the distribution of three fiber orientations at each voxel.

194 Given the use of Gd-DTPA and the absence of ex vivo T1w image, we inverted the contrast

195 of T2w or b0 image to obtain a fake T1w image (Ambrosen et al. 2020) which was then

196 preprocessed by the HCP-NHP pipeline (Autio et al. 2020), including warping the individual

197 volume image into the standard Yerks19 template (Donahue et al. 2018) using FSL, surface

8

198 construction using Freesurfer (https://surfer.nmr.mgh.harvard.edu/) and mapping the individual

199 space into the Yerk19 surface using the multimodal surface matching algorithm (Robinson et

200 al. 2014) (details in Fig. S1).

201 The T1w images of macaque in vivo TheVirtualBrain dataset were also preprocessed by

202 the HCP-NHP pipeline (details in Fig. S1).

203

204 **2.3 Definition of macaque insula ROI**

205 Our macaque insula ROI, mainly defined by the sulcus and gyrus, was delineated in a

206 postmortem macaque b0 template (CIVM) (Calabrese et al. 2015a) with labels of Paxinos et

207 al.'s macaque atlas (Paxinos et al. 2009) at the 0.3-mm isotropic resolution. More specifically,

208 first, we extracted the insula mask, including Ia, Id, Ig, and IPro (insular proisocortex), which

209 was defined in the CIVM atlas. This insula mask's ventral and dorsal extent was bounded by

210 the inferior and superior limiting sulcus of the insula, respectively, and its anterior extent

211 bordered ventrally on the piriform cortex. Second, we delineated the most anterior insula mask

212 with five regions, including Iam, Ial, Iapm, Iai and Iapl, which were defined in the D99 template

213 (Reveley et al. 2016) with labels of Saleem et al.'s macaque atlas (Saleem and Logothetis 2007).

214 These five regions were transformed from the D99 space into the CIVM space using ANTs. In

215 the CIVM space, the lateral extent of this mask was delimited by the inferior limiting of the

216 insula and its extended line, and the medial extent bordered posteriorly on the anterior olfactory

217 nucleus and medially piriform cortex. Finally, we merged these two masks into our macaque

218 insula ROI in the CIVM space, and the detailed volume ROI was shown in Fig. S2.

219

220 **2.4 Macaque insula SC gradients**

221 We aimed to construct a macaque insula connectome in the common volume space, a

222 symmetrical cross-correlation matrix, which could reveal the similarity of connectivity patterns

223 within voxels, and then be unveiled by the diffusion embedding to explore global insula spatial

224 distributions. For each ex vivo macaque brain, nonlinear registration (Avants et al. 2014) within

225 ANTs was applied to estimate a deformation field between the individual b0 image and CIVM

226 b0 template with an isotropic resolution of 0.3 mm. Given a decrease of the voxel number

227   transformed from the high-resolution b0 template to a low-resolution individual b0 image, we

228   resampled the macaque insula template mask into the 0.6-mm isotropic resolution, and then

229   labeled all the voxels within the insula mask from 1 to M. According to the estimated

230   deformation field, the insula mask was warped from the CIVM space with the isotropic

231   resolution of 0.6 mm into the individual space with a 0.45-mm isotropic resolution using

232   nearest-neighbor interpolation. In the individual space, the probability between each voxel in

233   the insula mask and the brain voxels (N) was calculated by the probabilistic tractography using

234   Probtrackx2 (Behrens et al. 2007) with the step length of 0.25 mm (Bryant et al. 2020) and

235   curvature threshold of 0.2, and the pial surfaces generated in the previous HCP-NHP pipeline

236   were treated as a stop mask to prevent fiber tracking from crossing sulci. Five thousand

237   streamlines per insula voxel were tracked to calculate the connectivity profiles, and we

238   averaged the connectivity profiles of voxels with the same label one by one to obtain the

239   individual M-by-N matrix. Then, a cross-correlation M-by-M matrix was calculated to reveal

240   the similarity between the voxels with different labels. Finally, we averaged all the subjects

241   cross-correlation matrices to obtain a group-level cross-correlation M-by-M matrix with the

242   min-max normalization.

243   A diffusion map algorithm (Berry and Harlim 2016) was applied to the group-level cross-

244   correlation matrix to obtain ten gradients of insula. The variance was calculated within each

245   gradient and normalized to acquire the explained variance of the gradient. The gradients in the

246   CIVM space were warped into the Yerks19 space using nonlinear registration within ANTs. We

247   normalized each gradient in the volume space and then mapped it to the 32k Yerks19 surface

248   for display using Connectome Workbench (https://www.humanconnectome.org/).

249

250   **2.5 SC-based parcellation**

251   In the CIVM space, we extracted the top and bottom 25% of all insula voxels in the dominant

252   gradient, and also extracted the top and bottom 25% of the rest insula voxels in the second

253   gradient. The four components were treated as the ROIs, which were subdivided using the SC-

254   based parcellation frame (Fan et al. 2016). The main steps can be summarized as follows: first,

255   the ROI was warped from the CIVM space into the individual space using the estimated

256   deformation field. Second, individual pial surfaces were conducted as the stopping mask, and

257   5000 streamlines per voxel in the individual ROI were tracked to construct the connectivity

258   matrix between the ROI and brain voxels using Probtrackx2. Third, in the individual space, we

259   obtained the cross-correlation matrix by multiplying the connectivity matrix by its transpose,

260   which was used as an input to the spectral clustering algorithm (Ng et al. 2002). Fourth, cluster

261   number was set from 2 to 6 and the individual parcellation results were warped into the CIVM

262   space. Finally, for each cluster solution, the maximum probabilistic map of one subregion was

263   acquired by identifying that the probability of voxel belonging to the subregion is more than

264   50% across the subjects. Additionally, to avoid the arbitrary selection of clusters, the cross-

265   validation indices Cramer's V and topological distance (TpD) (Li et al. 2017) were calculated

266   to choose the optimal cluster across all subjects.

267

268   **2.6 SC pattern**

269   After obtaining four components from the insula gradients and subregions from the subdivision

270   on the component, we characterized their connectivity profiles using the probabilistic tracking

271   strategy used in the SC parcellation. For the component or subregion, 50000 samples per voxel

272   were tracked to the whole brain using Probtrackx2, and also the pial surfaces were served as

273   the stop mask. For each subject, the connectivity profile of one component or subregion was

274   only focused on the ipsilateral hemisphere and transformed into the CIVM space. To further

275   reduce the false positive connections, 3.08×10^{-5} for the samples (He et al. 2020) was used to

276   binarize the connectivity profile. We averaged connectivity profiles of the subregion across the

277   subjects to get the probabilistic connectivity profile, and the threshold 0.5 was used to obtain

278   the group-level connectivity profile for the given subregion.

279   Meanwhile, we also performed connectivity fingerprints (Passingham et al. 2002) to reveal

280   the connectivity pattern between insula component or subregion and ipsilateral target ROIs.

281   The main procedures were summarized as follows: first, all cortical and subcortical regions in

282   the CIVM atlas with Paxinos et al.'s labels of macaque atlas (Paxinos et al. 2009) were extracted

283   as the target ROIs. Second, after obtaining the connectivity profiles thresholded in the CIVM

284   space, the connectivity values were calculated by averaging the voxel values within all the

11

285 target ROIs for each component or subregion, and then we averaged the connectivity values

286 across the subjects to obtain the initial connectivity fingerprints. Third, for all components or

287 subregions, we thresholded the connectivity fingerprints at >0.001 and then merged some

288 regions with similar connectivity patterns into one homogenous region. For example, area 10

289 and its dorsal, medial, ventral part were merged into one target ROI. Thus, a target ROI family

290 was generated, containing 29 cortical and 6 subcortical regions (details in Tabel S1). Fourth,

291 in the one subject, we recalculated the connectivity fingerprints using the new target ROIs

292 family again for all the components or subregions with the previous step 2. The connectivity

293 fingerprints of one subject were normalized by summing all the connections to 1 (Mars et al.

294 2012; Xia et al. 2017) within one component or subregion in all target ROIs and subsequently

295 within all the components or subregions in one target ROI. Finally, the connectivity fingerprints

296 of the components or subregions were constructed by averaging the individual normalized

297 connectivity fingerprints across the subjects.

298   A permutation test (Mars et al. 2016) was performed to investigate the difference of

299 connectivity fingerprints between the two subregions that originated from the component

300 subdivisions. More specifically, after obtaining the normalized fingerprints of all subjects, we

301 calculated the Manhattan distance between the connectivity fingerprints of the two subregions

302 with 35 targets ROIs within all subjects to characterize the observed difference between the

303 connectivity patterns of the two subregions. The hypothesis is that the difference between the

304 connectivity patterns of the two subregions was higher than expected by chance. Subsequently,

305 the Manhattan distances between the subregions were calculated for the 10000 permutations

306 for connectivity fingerprints of two subregions. If the observed Manhattan distance was higher

307 than the criterion derived from the permutation test ($p < 0.05$), the two subregions subdivided

308 from the component would show significant differences in the connectivity pattern.

309

310 **2.7 Relation to the T1w/T2w and cortical thickness map**

311 The cortical thickness maps in the Yerks19 space (Donahue et al. 2018) were generated by the

312 HCP-NHP pipeline in the macaque in vivo dataset. By averaging the cortical thickness maps

313 across the subjects, we obtained the group-level cortical thickness map. The correlation

12

314 analysis was performed to investigate the relationship between the insula dominant gradients

315 and the insula cortical thickness maps by the vertex values of the insula in the Yerks19 space.

316 To explore the relationship between insula SC gradients and T1w/T2w map, we used the

317 standard T1w/T2w map in the HCP-NHP pipeline, and then separated and resampled it into the

318 32k space using Connectome Workbench. Likewise, the correlation analysis was performed to

319 investigate the relationship between the insula dominant gradients and T1w/T2w maps.

320

321 **3. Results**

322 **3.1 SC gradients of macaque insula**

323 Based on the macaque insula SC connectome, diffusion maps revealed global spatial

324 distributions of the insular cortex where the top two insula gradients explained the variance

325 over 50% in total. We only focused on the top two gradients, and the others explained the

326 variance all below 10%. The dominant gradient (G1) explained 45.7% and 41.5% variance of

327 the left and right insula respectively (Fig. 1A). It showed a gradual increase along the

328 rostrocaudal axis (Fig. 1B, top). The second gradient (G2), accounting for 16.0% and 15.1%

329 variance for the left and right insula (Fig. 1A), showed the highest proportion in the middle

330 insula and a gradual decrease from the middle to the rostral and caudal direction separately

331 (Fig. 1B, bottom).

332

333 **3.2 Parcellation of macaque insula based on SC gradients**

334 The four components (INS1-4), including the top and bottom 25% of G1 and the additional top

335 and bottom 25% of G2, were extracted and merged into the initial partition of the insula with

336 the parallel rostral to the caudal pattern (Fig. 2A). With the highest CV and TpD indices, these

337 four components from INS1 to INS4 were all subdivided into two subregions (Fig. 2B),

338 including anteromedial and anterolateral Ia (Iaam and Iaal), posterodorsal and posteroventral

339 Ia (Iapd and Iapv), dorsal and ventral Id (Idd and Idv), and dorsal and ventral Ig (Igd and Igv)

340 (Fig. 2C).

341

342 **3.3 SC fingerprint of macaque insula subregion**

13

343   INS1, adjacent to area 13 medially, was located in the rostral part of the macaque insula, and

344   was subdivided into two subregions, including the medial portion Iaam and the lateral portion

345   Iaal (Fig. 2B). INS1 had strong ipsilateral connections with area 10, 46, 47, 11, 13, 14, 25, 32,

346   36R, TP and subcortical regions Acb, Str, Amyg, Pir (Fig. 3A). Using permutation tests, the

347   two subregions showed significant differences (LH: $p < 0.0001$, RH: $p < 0.0001$) in the

348   connectivity fingerprints and Iaam showed higher connections with area 14, 25, 36R, and Pir,

349   whereas area 10, 46, 47, 11, 13, 32, Tha, Acb and Amyg had higher connections with Iaal (Fig.

350   4A).

351   INS2 covered the anterior domain of the middle insula just posterior to INS1, which was

352   parcellated into two subregions, including the dorsal portion Iapd and the ventral portion Iapv

353   (Fig. 2B). INS2 had high ipsilateral connections with area ProM, Gu, 25, PaI, STS, TP and

354   subcortical regions Tha, Pir, Str, Pd (Fig. 3B). Significant differences (LH: $p < 0.0001$, RH: p

355   < 0.0001) were also found by permutation tests between the connectivity fingerprints of these

356   two subregions. Iapd had higher connections with area ProM, Gu, 6VR, 2/1, Tha, and Pd,

357   whereas area PPt, 36R, MST, PaA, PaI, STS, TP and Amyg showed higher connections with

358   Iapv (Fig. 4B).

359   INS3 occupied the posterior domain of the middle insula just posterior to INS2, and was

360   subdivided into two subregions, including the dorsal portion Idd and the ventral portion Idv

361   (Fig. 2B). INS3 had strong ipsilateral connections with areas 44, 45, ProM, Gu, 6VR, 8AV, 2/1,

362   PE, PPt, S2, AK, MST, PaA, ProK, STS, TPt, and subcortical regions Tha, Pd (Fig. 3C).

363   Permutations tests identified significant differences (LH: $p < 0.0001$, RH: $p = 2.00 \times 10^{-4}$)

364   between connectivity fingerprints of these two subregions. Idd showed higher connections with

365   areas 44, 45, ProM, Gu, 6VR, 2/1, S2, Tha and Pd, whereas Idv had higher connections with

366   36R, AK, MST, ProK, STS, and TPt (Fig. 4C).

367   INS4, adjacent to the S2 and ProK laterally, was located in the posterior domain of the

368   insula and was parcellated into two subregions, including the dorsal portion Igd and the ventral

369   portion Igv (Fig. 2B). INS4 had strong ipsilateral connections with areas 44, 45, 6VR, 8AV, PE,

370   IPL, PPt, S2, AK, MST, PaA, ProK, ReI, TPt, and subcortical regions Tha, Pd (Fig. 3D).

371   Significant differences (LH: $p < 0.0001$, RH: $p < 0.0001$) were identified by permutation tests

14

372 between the connectivity fingerprints of these two subregions. Igd showed higher connections

373 with areas 44, 45, 6VR, 8AV, and S2, whereas area PE, PPt, AK, MST, PaA, ProK and ReI had

374 higher connections with Igv (Fig. 4D).

375

376 **3.4 Relationships between gradients and T1w/T2w, cortical thickness maps**

377 Macaque insula G1 correlated positively with insula T1w/T2w map (LH: $r = 0.46$, $p < 0.0001$;

378 RH: $r = 0.43$, $p < 0.0001$) (Fig. 5A), and negatively with insula thickness map (LH: $r = -0.31$,

379 $p < 0.0001$; RH: $r = -0.28$, $p < 0.0001$) (Fig. 5B). However, G2 correlated negatively with insula

380 T1w/T2w map (LH: $r = -0.43$, $p < 0.0001$; RH: $r = -0.40$, $p < 0.0001$) (Fig. 5A), and positively

381 with insula thickness map (LH: $r = 0.26$, $p < 1.16e-14$; RH: $r = 0.29$, $p < 6.31e-19$) (Fig. 5B).

382

383 **4. Discussion**

384 Based on structural connectivity, this study investigated global gradients and subdivisions in

385 the macaque insular cortex and also explored the relationship between insula global gradients

386 and its morphology and microstructure. The insula G1 revealed the gradually rostrocaudal

387 increases, whereas the insula G2 represented gradual increases from the rostral and caudal

388 portions to the middle domain. Extracting four components from the first two insula gradients,

389 a connectivity-based parcellation method was performed to subdivide each component into two

390 subregions, showing medial-lateral or dorsal-ventral parcellation pattern. Moreover, these two

391 subregions showed significant differences between their connectivity fingerprints by

392 permutation tests. In addition, insula gradients also captured the characteristics of T1w/T2w

393 and thickness maps. Overall, macaque insula gradients or subdivisions using neuroimaging

394 provided insights to comparative or translational medicine research.

395

396 **4.1 Macaque insula gradients and parcellations**

397 We examined the spatial representation of structural connectivity variation across macaque

398 insula territory and found a rostrocaudal gradient (Fig. 6A top). This result was similar to a

399 cytoarchitectonic study with multiple stains reporting that parallel ventral to dorsal gradients

400 were found in the middle layer of the macaque insula (Fig. 6B) (Gallay et al. 2012b). Our result

15

401 was consistent with a human neuroimaging study showing that probabilistic tractography

402 uncovered a rostrocaudal trajectory of connectivity variability in the human insula (Cerliani et

403 al. 2012a). However, the comparability across species is not clear and requires further

404 examination. Besides, we constituted a 4-subregion parcellation pattern by extracting the top

405 and bottom 25% components from the first two gradients instead of directly hard clustering

406 algorithms to subdivide macaque insula. Given the unstable boundaries in the middle insula by

407 the hard clustering reported in a previous study (Nanetti et al. 2009), such extract method

408 making up 4-subregion pattern could guarantee that the two subregions from one insula

409 gradient represented the maximum connectivity variations. More interestingly, the three

410 subregions INS2-4 posterior to the limen insula in the 4-subregion pattern spatially arranged

411 by a cytoarchitectonic study of the macaque insula with an anteroposterior parcellation (Fig.

412 6C) (Calabrese et al. 2015a; Paxinos et al. 2009). Moreover, the subdivision of INS2, which

413 was parcellated into Iapd and Iapv, was similar to the Ia and IPro in the Paxinos et al.'s macaque

414 atlas that Ia showed more SMI reactivity than IPro in the infragranular layers (Paxinos et al.

415 2009). In case of these three subregions, the subdivision results all revealed the ventrodorsal

416 pattern, similar to the cytoarchitectonic study showing the dorsal and ventral architectonic areas

417 of the macaque posterior insula (Fig. 6D) (Evrard et al. 2014). Concerning the subregion INS1

418 in the posterior surface of the orbitofrontal lobe, the subdivision of this region showed a medial-

419 lateral pattern which also corresponded to a previous histology study subdividing the

420 proportion of insula anterior to limen insula into Iam, Iai, Ial, Iapm, and Iapl (Carmichael and

421 Price 1994b). Taken together, our results revealed the structural organization of macaque insula,

422 showing from the global anteroposterior gradient pattern to the mediolateral or ventrodorsal

423 subdivision pattern locally, which were both consistent with the previous cytoarchitectonic

424 studies on macaque insula.

425

426 **4.2 Macaque insula SC**

427 Apart from research on the structural organization of macaque insula, the present study also

428 investigated the structural connectivity of the insula subregions. INS1 had strong structural

429 connectivity with the lateral prefrontal cortex, orbitofrontal cortex, anterior cingulate gyrus,

430   perirhinal cortex, Pir, and Acb. More specifically, the lateral subregion Iaal, subdivided from

431   the INS1, showed higher connections with areas 10, 46, 47, 32, 11, 13, and Acb, whereas the

432   medial subregion Iaam connected strongly with area 14, 25, and Pir. The previous tracer study

433   reported anatomical connections between area 10 and the posterior orbitofrontal lobe (Petrides

434   and Pandya 2007). The macaque frontal pole was thought to play a critical role in cognitive

435   processing, such as complex and higher-order behaviors (Boschin et al. 2015). Previous lesion

436   studies (Murphy and Bachevalier 2020) and tasks (Setogawa et al. 2019) revealed that

437   orbitofrontal areas 11, 47, and 13 played vital roles in the attention, reward and may also

438   participate in social behavior. Thus, the connections between Iaal and these regions may

439   indicate that the lateral subregion of INS1 was associated with the higher cognitive functions.

440   In addition, in one tracer study (Carmichael et al. 1994), Pir was connected with two

441   cytoarchitectonic insula areas (Iam and Iapm) corresponding to the subregion Iaam in our

442   research. Pir plays a vital role in the processing and encoding of olfactory information (Boyett-

443   Anderson et al. 2003), and area 14 also participants in olfactory-related function (Ongur and

444   Price 2000). Therefore, the medial subregion Iaam of INS1 may play an essential role in the

445   processing of olfactory information. For areas 25 and 32, the recent study suggested that these

446   two regions of the primate were involved in the opposite roles in regulating negative emotion,

447   such as the cardiovascular and behavioral correlates (Wallis et al. 2017). In our study, the two

448   subregions, Iaam and Iaal, showed high connections, respectively, with areas 25 and 32

449   indicating the different roles of the two subregions in the emotion regulations. INS1 plays a

450   crucial role in the higher cognitive functions and participants in the processing of olfactory

451   information.

452   This study, INS2 connected strongly with the ProM, Gu, PaI, STS, TP, Tha, and Amyg.

453   The dorsal subregion Iapd, parcelled from INS2, showed higher structural connectivity with

454   the ProM, Gu, and Tha, whereas the ventral subregion Iapv showed stronger SC with the Amyg.

455   Previous evidence considered that the taste pathway of the macaque brain contained the nucleus

456   of the solitary tract, thalamus, anterior insula, Gu, orbitofrontal cortex, amygdala, anterior

457   cingulate cortex, and hypothalamus (Rolls 2019). Thus, the INS2 was mainly responsible for

458   integrating taste information and participated in the feeding processing. A previous tracer study

459 reported that the TP region had anatomical connectivity with agranular, parainsular, and

460 dysgranular insula, the medial frontal, and orbitofrontal cortex, implicating the TP was

461 associated with the auditory-related memory processing (Corcoles-Parada et al. 2019). In our

462 study, Iapv, connected with TP and PaI, may participate in the auditory memory function.

463   The dorsal subregions Idd and Igd, subdivided from the INS3 and INS4 respectively, had

464 strong connections with 6VR, verified by a tracer study (Morecraft et al. 2015), reporting the

465 anatomical connectivity of the dysgranular insula with the ventral premotor area. In addition,

466 Idd and Igd showed strong connections with areas 44, 45, and IPL. The previous study (Petrides

467 and Pandya 2009) has considered that macaque areas 44 and 45 may be homologous to the

468 human Broc's area. The ventral premotor mainly controlled the hand (Kraskov et al. 2009) and

469 orofacial (Ferrari et al. 2003) musculature. IPL also was demonstrated by the recent study to

470 be homologous in the primate and was mainly involved in the tool use and language (Cheng et

471 al. 2021). Taken together, the Idd and Igd may be a participant in the hand control and orofacial

472 motor in the rhesus monkey, such as vocalization. In addition, the connections of Idd and Igd

473 also showed higher connections with areas 2/1 and S2, indicating that these two subregions

474 were mainly involved in the somatosensory functions. Concerning the ventral subregions of

475 INS3 and INS4, Idv and Igv both had higher connections with AK and PaA, indicating that

476 these two subregions were mainly responsible for integrating the auditory information, and

477 together with the abovementioned subregion Iapv, thus these three ventral subregions played

478 an vital role in the auditory function.

479

480 **4.3 Macaque insula gradient captures structural features**

481 After identifying the gradient of the macaque insula based on structural connectivity, we

482 investigated the underlying architectonic mechanisms of macaque insula microstructure and

483 morphology, discovering close correlations between insula thickness, T1w/T2w and

484 connectivity-based gradient. The macaque insular cortex was characterized by the lamination

485 pattern and also revealed by the architectonic gradient of cortical layers (Gallay et al. 2012a).

486 In neuroimaging, T1w/T2w ratio, detecting the architectonic organization, is a proxy for the

487 myelin content in the cortical regions. Moreover, the macaque insula has been considered to be

488   an inconsistent cortical area with a differentiated layer of myeline (Mesulam and Mufson 1982;

489   Evrard et al. 2014). Therefore, in this study, the relationship between the gradients and

490   T1w/T2w map indicated that the spatial distribution of connectivity variation was corresponded

491   to the myelination, suggesting that the macroscopic organization of the macaque insular cortex

492   may capture the underlying microstructural features to some extent. In addition, we also

493   detected the correlation between the gradient and thickness in the macaque insular cortex. This

494   finding was consistent with the previous finding that the gradient of human thalamus correlated

495   with its gray matter volume (Yang et al. 2020). The cortical thickness, measuring the depth of

496   the cortical column, was the macroscopic representation of the layer physical features, which

497   exhibited the incongruous characteristics in the macaque insula. Our finding, correlations of

498   gradient and thickness, may indicate that the variation of structural connectivity in the macaque

499   insular cortex was associated with its morphological structure. Overall, the relationship of

500   gradients, T1w/T2w and thickness suggested that the macro-structural organization of the

501   macaque insular cortex may be in accordance with its microstructure and morphology.

502

4.4 Limitations

503

504   Several limitations should be mentioned in the present study here. First, although the insula 4-

505   subregion parcellation pattern appeared to be similar to the previous histological studies by

506   extracting the 25% component from the global gradient, the chosen threshold was relatively

507   subjective and required further examination. Second, due to the lack of in vivo MRI data of

508   macaque brain collected by us, the correlation analysis on the relationship between the insula

509   gradient and thickness was not conducted on the MRI data of the same macaque brains, which

510   may influence our findings. Third, we did not construct the T1w/T2w map and just used the

511   existed template to explore the relationship between the insula gradient and the T1w/T2w map,

512   which weakened the interpretability of correlation analysis findings.

513

5. Conclusion

514

515   Using high-resolution ex vivo diffusion MRI data, this study revealed the topographic

516   organization of macaque insular cortex globally and locally based on structural connectivity.

517 The gradient and parcellation of the macaque insular cortex were both similar to the

518 histological architecture reported by the previous studies. Furthermore, permutation tests

519 associated with connectivity fingerprint were performed to confirm the subdivisions of 8

520 subregions parcellated from the 4 components. Besides, the relationships between insula

521 gradients and the T1w/T2w, thickness maps also suggested that the macroscopic connectivity

522 variation across the cortical territory in the macaque insula may capture the underlying

523 morphological and microstructural features. Overall, our study investigated macaque insula

524 architecture from the perspective of structural connectivity, which may provide an insight into

525 the following comparative research across species.

526

527 **Author contributions**

528 Tianzi Jiang led the project. Tianzi Jiang and Lingzhong Fan were responsible for the design

529 of the concept and study. Long Cao, Zhongchang Du and Yue Cui contributed to the writing,

530 coding, plotting and validation of the pipeline. All the authors participated in discussions of the

531 results and revision of the manuscript.

532

533 **Acknowledgments**

540

541 **Conflict of interest**

542 The authors declare that they have no conflict of interest.

543

544 **Data and code availability**

545 The data and codes that support the findings of this study are available from the corresponding

546   author upon reasonable request.

547

548   **References**

549   Ambrosen KS, Eskildsen SF, Hinne M, Krug K, Lundell H, Schmidt MN, van Gerven MAJ, Morup M,
550   Dyrby TB (2020) Validation of structural brain connectivity networks: The impact of scanning
551   parameters. Neuroimage 204:116207. https://doi:10.1016/j.neuroimage.2019.116207

552   Autio JA, Glasser MF, Ose T, Donahue CJ, Bastiani M, Ohno M, Kawabata Y, Urushibata Y, Murata K,
553   Nishigori K, Yamaguchi M, Hori Y, Yoshida A, Go Y, Coalson TS, Jbabdi S, Sotiropoulos SN,
554   Kennedy H, Smith S, Van Essen DC, Hayashi T (2020) Towards HCP-Style macaque connectomes:
555   24-Channel 3T multi -array coil, MRI sequences and preprocessing. Neuroimage 215.
556   https://doi:10.1016/j.neuroimage.2020.116800

557   Avants BB, Tustison NJ, Stauffer M, Song G, Wu B, Gee JC (2014) The Insight ToolKit image registration
558   framework. Front Neuroinform 8:44. https://doi:10.3389/fninf.2014.00044

559   Behrens TE, Berg HJ, Jbabdi S, Rushworth MF, Woolrich MW (2007) Probabilistic diffusion tractography
560   with multiple fibre orientations: What can we gain? Neuroimage 34 (1):144-155.
561   https://doi:10.1016/j.neuroimage.2006.09.018

562   Berry T, Harlim J (2016) Variable bandwidth diffusion kernels. Appl Comput Harmon A 40 (1):68-96.
563   https://doi:10.1016/j.acha.2015.01.001

564   Boschin EA, Piekema C, Buckley MJ (2015) Essential functions of primate frontopolar cortex in cognition.
565   Proc Natl Acad Sci U S A 112 (9):E1020-1027. https://doi:10.1073/pnas.1419649112

566   Boyett-Anderson JM, Lyons DM, Reiss AL, Schatzberg AF, Menon V (2003) Functional brain imaging of
567   olfactory processing in monkeys. Neuroimage 20 (1):257-264. https://doi:10.1016/s1053-
568   8119(03)00288-x

569   Bryant KL, Li L, Eichert N, Mars RB (2020) A comprehensive atlas of white matter tracts in the chimpanzee.
570   PLoS Biol 18 (12):e3000971. https://doi:10.1371/journal.pbio.3000971

571   Calabrese E, Badea A, Coe CL, Lubach GR, Shi Y, Styner MA, Johnson GA (2015a) A diffusion tensor MRI
572   atlas of the postmortem rhesus macaque brain. Neuroimage 117:408-416.
573   https://doi:10.1016/j.neuroimage.2015.05.072

574   Calabrese E, Badea A, Coe CL, Lubach GR, Shi YD, Styner MA, Johnson GA (2015b) A diffusion tensor
575   MRI atlas of the postmortem rhesus macaque brain. Neuroimage 117:408-416.
576   https://doi:10.1016/j.neuroimage.2015.05.072

577   Carmichael ST, Clugnet MC, Price JL (1994) Central olfactory connections in the macaque monkey. J Comp
578   Neurol 346 (3):403-434. https://doi:10.1002/cne.903460306

579   Carmichael ST, Price JL (1994a) Architectonic Subdivision of the Orbital and Medial Prefrontal Cortex in
580   the Macaque Monkey. Journal of Comparative Neurology 346 (3):366-402. https://doi:DOI
581   10.1002/cne.903460305

582   Carmichael ST, Price JL (1994b) Architectonic subdivision of the orbital and medial prefrontal cortex in the
583   macaque monkey. J Comp Neurol 346 (3):366-402. https://doi:10.1002/cne.903460305

584   Caruana F, Jezzini A, Sbriscia-Fioretti B, Rizzolatti G, Gallese V (2011) Emotional and social behaviors
585   elicited by electrical stimulation of the insula in the macaque monkey. Curr Biol 21 (3):195-199.
586   https://doi:10.1016/j.cub.2010.12.042

587   Cerliani L, Thomas RM, Jbabdi S, Siero JC, Nanetti L, Crippa A, Gazzola V, D'Arceuil H, Keysers C (2012a)
588   Probabilistic tractography recovers a rostrocaudal trajectory of connectivity variability in the human
589   insular cortex. Hum Brain Mapp 33 (9):2005-2034. https://doi:10.1002/hbm.21338

590 Cerliani L, Thomas RM, Jbabdi S, Siero JCW, Nanetti L, Crippa A, Gazzola V, D'Arceuil H, Keysers C
591   (2012b) Probabilistic tractography recovers a rostrocaudal trajectory of connectivity variability in
592   the human insular cortex. Human Brain Mapping 33 (9):2005-2034. https://doi:10.1002/hbm.21338

593 Cheng L, Zhang Y, Li G, Wang J, Sherwood C, Gong G, Fan L, Jiang T (2021) Connectional asymmetry of
594   the inferior parietal lobule shapes hemispheric specialization in humans, chimpanzees, and rhesus
595   macaques. Elife 10. https://doi:10.7554/eLife.67600

596 Corcoles-Parada M, Ubero-Martinez M, Morris RGM, Insausti R, Mishkin M, Munoz-Lopez M (2019)
597   Frontal and Insular Input to the Dorsolateral Temporal Pole in Primates: Implications for Auditory
598   Memory. Front Neurosci 13:1099. https://doi:10.3389/fnins.2019.01099

599 D'Arceuil HE, Westmoreland S, de Crespigny AJ (2007) An approach to high resolution diffusion tensor
600   imaging in fixed primate brain. Neuroimage 35 (2):553-565.
601   https://doi:10.1016/j.neuroimage.2006.12.028

602 Di Cesare G, Pinardi C, Carapelli C, Caruana F, Marchi M, Gerbella M, Rizzolatti G (2019) Insula
603   Connections With the Parieto-Frontal Circuit for Generating Arm Actions in Humans and Macaque
604   Monkeys. Cereb Cortex 29 (5):2140-2147. https://doi:10.1093/cercor/bhy095

605 Donahue CJ, Glasser MF, Preuss TM, Rilling JK, Van Essen DC (2018) Quantitative assessment of prefrontal
606   cortex in humans relative to nonhuman primates. Proc Natl Acad Sci U S A 115 (22):E5183-E5192.
607   https://doi:10.1073/pnas.1721653115

608 Evrard HC (2019) The Organization of the Primate Insular Cortex. Front Neuroanat 13:43.
609   https://doi:10.3389/fnana.2019.00043

610 Evrard HC, Forro T, Logothetis NK (2012) Von Economo neurons in the anterior insula of the macaque
611   monkey. Neuron 74 (3):482-489. https://doi:10.1016/j.neuron.2012.03.003

612 Evrard HC, Logothetis NK, Craig AD (2014) Modular architectonic organization of the insula in the
613   macaque monkey. J Comp Neurol 522 (1):64-97. https://doi:10.1002/cne.23436

614 Fan L, Li H, Zhuo J, Zhang Y, Wang J, Chen L, Yang Z, Chu C, Xie S, Laird AR, Fox PT, Eickhoff SB, Yu
615   C, Jiang T (2016) The Human Brainnetome Atlas: A New Brain Atlas Based on Connectional
616   Architecture. Cereb Cortex 26 (8):3508-3526. https://doi:10.1093/cercor/bhw157

617 Ferrari PF, Gallese V, Rizzolatti G, Fogassi L (2003) Mirror neurons responding to the observation of
618   ingestive and communicative mouth actions in the monkey ventral premotor cortex. European
619   Journal of Neuroscience 17 (8):1703-1714. https://doi:10.1046/j.1460-9568.2003.02601.x

620 Gallay DS, Gallay MN, Jeanmonod D, Rouiller EM, Morel A (2012a) The Insula of Reil Revisited:
621   Multiarchitectonic Organization in Macaque Monkeys. Cerebral Cortex 22 (1):175-190.
622   https://doi:10.1093/cercor/bhr104

623 Gallay DS, Gallay MN, Jeanmonod D, Rouiller EM, Morel A (2012b) The insula of Reil revisited:
624   multiarchitectonic organization in macaque monkeys. Cereb Cortex 22 (1):175-190.
625   https://doi:10.1093/cercor/bhr104

626 Graham MS, Drobnjak I, Zhang H (2016) Realistic simulation of artefacts in diffusion MRI for validating
627   post-processing correction techniques. Neuroimage 125:1079-1094.
628   https://doi:10.1016/j.neuroimage.2015.11.006

629 He B, Cao L, Xia X, Zhang B, Zhang D, You B, Fan L, Jiang T (2020) Fine-Grained Topography and
630   Modularity of the Macaque Frontal Pole Cortex Revealed by Anatomical Connectivity Profiles.
631   Neurosci Bull 36 (12):1454-1473. https://doi:10.1007/s12264-020-00589-1

632 Jbabdi S, Sotiropoulos SN, Savio AM, Grana M, Behrens TEJ (2012) Model-based analysis of multishell
633   diffusion MR data for tractography: How to get over fitting problems. Magnetic Resonance in

634 Medicine 68 (6):1846-1855. https://doi:10.1002/mrm.24204

635 Jenkinson M, Beckmann CF, Behrens TE, Woolrich MW, Smith SM (2012) Fsl. Neuroimage 62 (2):782-790.
636 https://doi:10.1016/j.neuroimage.2011.09.015

637 Jezzini A, Caruana F, Stoianov I, Gallese V, Rizzolatti G (2012) Functional organization of the insula and
638 inner perisylvian regions. Proc Natl Acad Sci U S A 109 (25):10077-10082.
639 https://doi:10.1073/pnas.1200143109

640 Kellner E, Dhital B, Kiselev VG, Reisert M (2016) Gibbs-Ringing Artifact Removal Based on Local
641 Subvoxel-Shifts. Magnetic Resonance in Medicine 76 (5):1574-1581.
642 https://doi:10.1002/mrm.26054

643 Kraskov A, Dancause N, Quallo MM, Shepherd S, Lemon RN (2009) Corticospinal neurons in macaque
644 ventral premotor cortex with mirror properties: a potential mechanism for action suppression?
645 Neuron 64 (6):922-930. https://doi:10.1016/j.neuron.2009.12.010

646 Li H, Fan L, Zhuo J, Wang J, Zhang Y, Yang Z, Jiang T (2017) ATPP: A Pipeline for Automatic Tractography-
647 Based Brain Parcellation. Front Neuroinform 11:35. https://doi:10.3389/fninf.2017.00035

648 Mars RB, Sallet J, Schuffelgen U, Jbabdi S, Toni I, Rushworth MF (2012) Connectivity-based subdivisions
649 of the human right "temporoparietal junction area": evidence for different areas participating in
650 different cortical networks. Cereb Cortex 22 (8):1894-1903. https://doi:10.1093/cercor/bhr268

651 Mars RB, Verhagen L, Gladwin TE, Neubert FX, Sallet J, Rushworth MF (2016) Comparing brains by
652 matching connectivity profiles. Neurosci Biobehav Rev 60:90-97.
653 https://doi:10.1016/j.neubiorev.2015.10.008

654 Menon V, Gallardo G, Pinsk MA, Nguyen VD, Li JR, Cai W, Wassermann D (2020) Microstructural
655 organization of human insula is linked to its macrofunctional circuitry and predicts cognitive control.
656 Elife 9. https://doi:10.7554/eLife.53470

657 Mesulam MM, Mufson EJ (1982) Insula of the old world monkey. I. Architectonics in the insulo-orbito-
658 temporal component of the paralimbic brain. J Comp Neurol 212 (1):1-22.
659 https://doi:10.1002/cne.902120102

660 Mizuhiki T, Richmond BJ, Shidara M (2012) Encoding of reward expectation by monkey anterior insular
661 neurons. J Neurophysiol 107 (11):2996-3007. https://doi:10.1152/jn.00282.2011

662 Morecraft RJ, Stilwell-Morecraft KS, Ge J, Cipolloni PB, Pandya DN (2015) Cytoarchitecture and cortical
663 connections of the anterior insula and adjacent frontal motor fields in the rhesus monkey. Brain Res
664 Bull 119 (Pt A):52-72. https://doi:10.1016/j.brainresbull.2015.10.004

665 Murphy LE, Bachevalier J (2020) Damage to Orbitofrontal Areas 12 and 13, but Not Area 14, Results in
666 Blunted Attention and Arousal to Socioemotional Stimuli in Rhesus Macaques. Front Behav
667 Neurosci 14:150. https://doi:10.3389/fnbeh.2020.00150

668 Nanetti L, Cerliani L, Gazzola V, Renken R, Keysers C (2009) Group analyses of connectivity-based cortical
669 parcellation using repeated k-means clustering. Neuroimage 47 (4):1666-1677.
670 https://doi:10.1016/j.neuroimage.2009.06.014

671 Ng AY, Jordan MI, Weiss Y (2002) On spectral clustering: Analysis and an algorithm. Advances in Neural
672 Information Processing Systems 14, Vols 1 and 2 14:849-856

673 Ongur D, Price JL (2000) The organization of networks within the orbital and medial prefrontal cortex of
674 rats, monkeys and humans. Cereb Cortex 10 (3):206-219

675 Passingham RE, Stephan KE, Kotter R (2002) The anatomical basis of functional localization in the cortex.
676 Nat Rev Neurosci 3 (8):606-616. https://doi:10.1038/nrn893

677 Paxinos G, Huang XF, Petrides M, Toga AW (2009) The rhesus monkey brain in stereotaxic coordinates.

678   2nd ed. Academic Press, San Diego

679 Petrides M, Pandya DN (2007) Efferent association pathways from the rostral prefrontal cortex in the
680   macaque monkey. J Neurosci 27 (43):11573-11586. https://doi:10.1523/JNEUROSCI.2419-
681   07.2007

682 Petrides M, Pandya DN (2009) Distinct parietal and temporal pathways to the homologues of Broca's area
683   in the monkey. PLoS Biol 7 (8):e1000170. https://doi:10.1371/journal.pbio.1000170

684 Remedios R, Logothetis NK, Kayser C (2009) An auditory region in the primate insular cortex responding
685   preferentially to vocal communication sounds. J Neurosci 29 (4):1034-1045.
686   https://doi:10.1523/JNEUROSCI.4089-08.2009

687 Reveley C, Gruslys A, Ye FQ, Glen D, Samaha J, B ER, Saad Z, A KS, Leopold DA, Saleem KS (2016)
688   Three-Dimensional Digital Template Atlas of the Macaque Brain. Cereb Cortex.
689   https://doi:10.1093/cercor/bhw248

690 Robinson EC, Jbabdi S, Glasser MF, Andersson J, Burgess GC, Harms MP, Smith SM, Van Essen DC,
691   Jenkinson M (2014) MSM: a new flexible framework for Multimodal Surface Matching.
692   Neuroimage 100:414-426. https://doi:10.1016/j.neuroimage.2014.05.069

693 Rolls ET (2019) Taste and smell processing in the brain. Handb Clin Neurol 164:97-118.
694   https://doi:10.1016/B978-0-444-63855-7.00007-1

695 Royer J, Paquola C, Lariviere S, Vos de Wael R, Tavakol S, Lowe AJ, Benkarim O, Evans AC, Bzdok D,
696   Smallwood J, Frauscher B, Bernhardt BC (2020) Myeloarchitecture gradients in the human insula:
697   Histological underpinnings and association to intrinsic functional connectivity. Neuroimage
698   216:116859. https://doi:10.1016/j.neuroimage.2020.116859

699 Saleem KS, Logothetis N (2007) A combined MRI and histology atlas of the rhesus monkey brain in
700   stereotaxic coordinates. Academic, London ; Burlington, MA

701 Setogawa T, Mizuhiki T, Matsumoto N, Akizawa F, Kuboki R, Richmond BJ, Shidara M (2019) Neurons in
702   the monkey orbitofrontal cortex mediate reward value computation and decision-making. Commun
703   Biol 2:126. https://doi:10.1038/s42003-019-0363-0

704 Shen K, Bezgin G, Schirner M, Ritter P, Everling S, McIntosh AR (2019) A macaque connectome for large-
705   scale network simulations in TheVirtualBrain. Sci Data 6 (1):123. https://doi:10.1038/s41597-019-
706   0129-z

707 Smith SM (2002) Fast robust automated brain extraction. Human Brain Mapping 17 (3):143-155.
708   https://doi:10.1002/hbm.10062

709 Smith SM, Jenkinson M, Woolrich MW, Beckmann CF, Behrens TE, Johansen-Berg H, Bannister PR, De
710   Luca M, Drobnjak I, Flitney DE, Niazy RK, Saunders J, Vickers J, Zhang Y, De Stefano N, Brady
711   JM, Matthews PM (2004) Advances in functional and structural MR image analysis and
712   implementation as FSL. Neuroimage 23 Suppl 1:S208-219.
713   https://doi:10.1016/j.neuroimage.2004.07.051

714 Tian Y, Zalesky A (2018) Characterizing the functional connectivity diversity of the insula cortex:
715   Subregions, diversity curves and behavior. Neuroimage 183:716-733.
716   https://doi:10.1016/j.neuroimage.2018.08.055

717 Tournier JD, Smith R, Raffelt D, Tabbara R, Dhollander T, Pietsch M, Christiaens D, Jeurissen B, Yeh CH,
718   Connelly A (2019) MRtrix3: A fast, flexible and open software framework for medical image
719   processing and visualisation. Neuroimage 202. https://doi:10.1016/j.neuroimage.2019.116137

720 Tustison NJ, Avants BB, Cook PA, Zheng Y, Egan A, Yushkevich PA, Gee JC (2010) N4ITK: improved N3
721   bias correction. IEEE Trans Med Imaging 29 (6):1310-1320.

722   https://doi:10.1109/TMI.2010.2046908

723 Van Essen DC (2002) Windows on the brain: the emerging role of atlases and databases in neuroscience.
724   Curr Opin Neurobiol 12 (5):574-579. https://doi:10.1016/s0959-4388(02)00361-6

725 Veraart J, Novikov DS, Christiaens D, Ades-Aron B, Sijbers J, Fieremans E (2016) Denoising of diffusion
726   MRI using random matrix theory. Neuroimage 142:384-396.
727   https://doi:10.1016/j.neuroimage.2016.08.016

728 Wallis CU, Cardinal RN, Alexander L, Roberts AC, Clarke HF (2017) Opposing roles of primate areas 25
729   and 32 and their putative rodent homologs in the regulation of negative emotion. P Natl Acad Sci
730   USA 114 (20):E4075-E4084. https://doi:10.1073/pnas.1620115114

731 Woolrich MW, Jbabdi S, Patenaude B, Chappell M, Makni S, Behrens T, Beckmann C, Jenkinson M, Smith
732   SM (2009) Bayesian analysis of neuroimaging data in FSL. Neuroimage 45 (1 Suppl):S173-186.
733   https://doi:10.1016/j.neuroimage.2008.10.055

734 Xia XL, Fan LZ, Cheng C, Eickhoff SB, Chen JJ, Li HF, Jiang TZ (2017) Multimodal connectivity-based
735   parcellation reveals a shell-core dichotomy of the human nucleus accumbens. Human Brain
736   Mapping 38 (8):3878-3898. https://doi:10.1002/hbm.23636

737 Yang S, Meng Y, Li J, Li B, Fan YS, Chen H, Liao W (2020) The thalamic functional gradient and its
738   relationship to structural basis and cognitive relevance. Neuroimage 218:116960.
739   https://doi:10.1016/j.neuroimage.2020.116960

740 Yaxley S, Rolls ET, Sienkiewicz ZJ (1990) Gustatory responses of single neurons in the insula of the
741   macaque monkey. J Neurophysiol 63 (4):689-700. https://doi:10.1152/jn.1990.63.4.689

742

Figure legends

Figure 1. Macaque insula gradients based on structural connectivity. (A) Ten insula gradients distribution and their variance explained. (B) The top two insula gradients mapped into Yerks19 surface space. The gradients were normalized to the maximum value in the range of 0 to 1 for visualization.

Figure 2. Subdivisions of macaque insula. (A) Initial insula partition merged from the dominant and second gradient with top and bottom 25% portion. (B) Validation indices and subdivisions in 2 clusters for all four components. Cramer's V (CV) described consistency of parcellation across subjects, and topological distance (TpD) measured the symmetry of parcellations between hemispheres. Higher values of CV and TpD indicated good consistency and symmetry, respectively. (C) The final insula subdivision with 8 subregions.

Figure 3. The connectivity patterns of four components, including INS1 (A), INS2 (B), INS3 (C), and INS4 (D). The connectivity profile was mapped into the F99 surface space (Van Essen 2002) for visualization using Caret5 and focused on the ipsilateral hemisphere.

Figure 4. Connectivity patterns of each two subregions subdivided from four components INS1 (A), INS2 (B), INS3 (C), and INS4 (D). Connectivity profiles focused on the ipsilateral hemisphere for one subregion. Permutation tests (histograms) were used to identify differences between connectivity fingerprints of two subregions. The observations, the Manhattan distance between two fingerprints, was higher than the criterion of permutations, indicating significant differences between the connectivity fingerprints of two subregions.

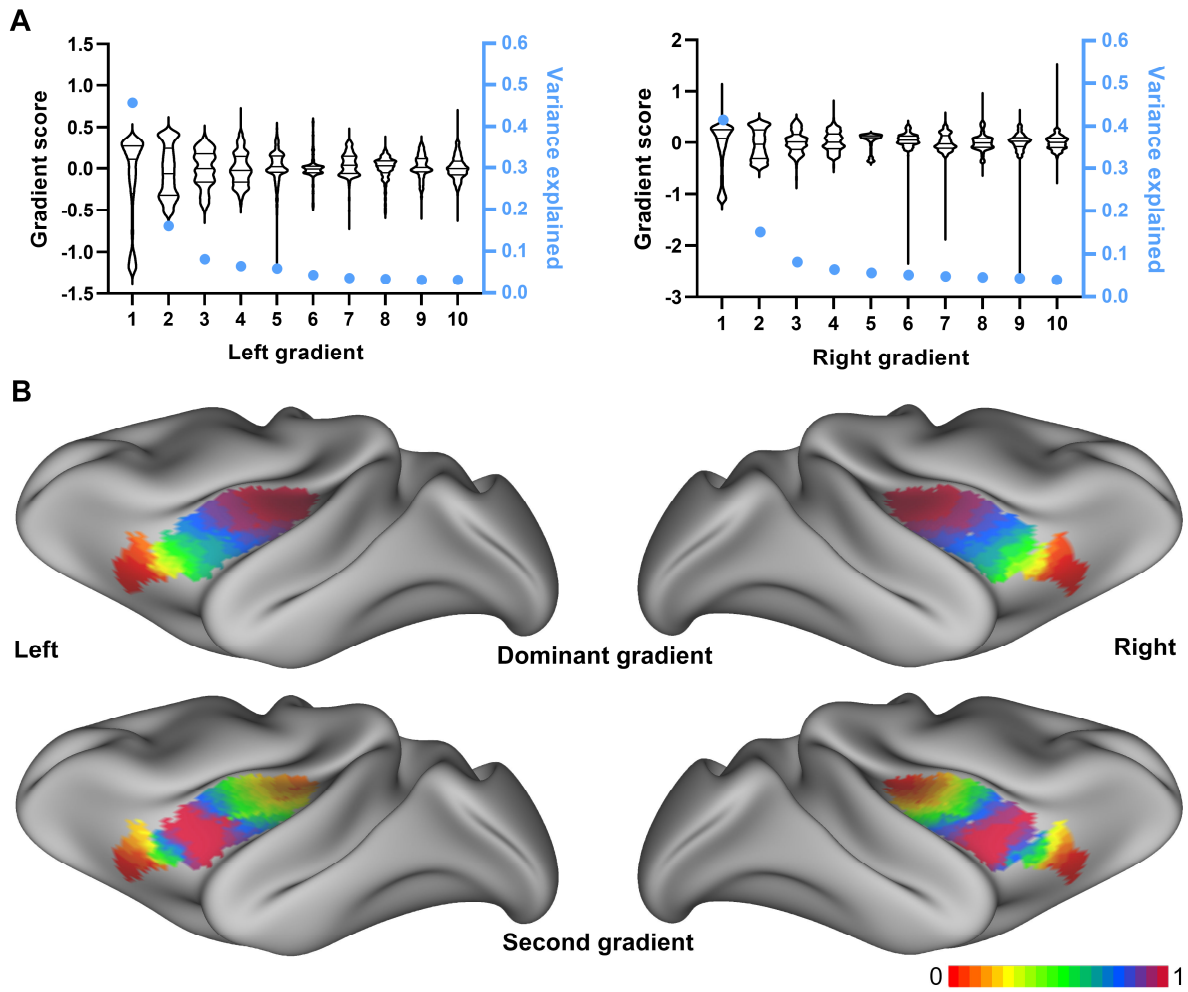**Figure 5.** Insula gradients captured insula microstructure and morphology. (A) Insula gradients revealed the significant correlations with T1w/T2w map. (B) Insula gradients were associated with cortical thickness.

Figure 6. Comparison between macaque insula topographic organization in our study and the prior insula histological architecture. (A) Insula topographic organization. From top to bottom, macaque insula was obtained by structural connectivity gradients, 25% components extraction,
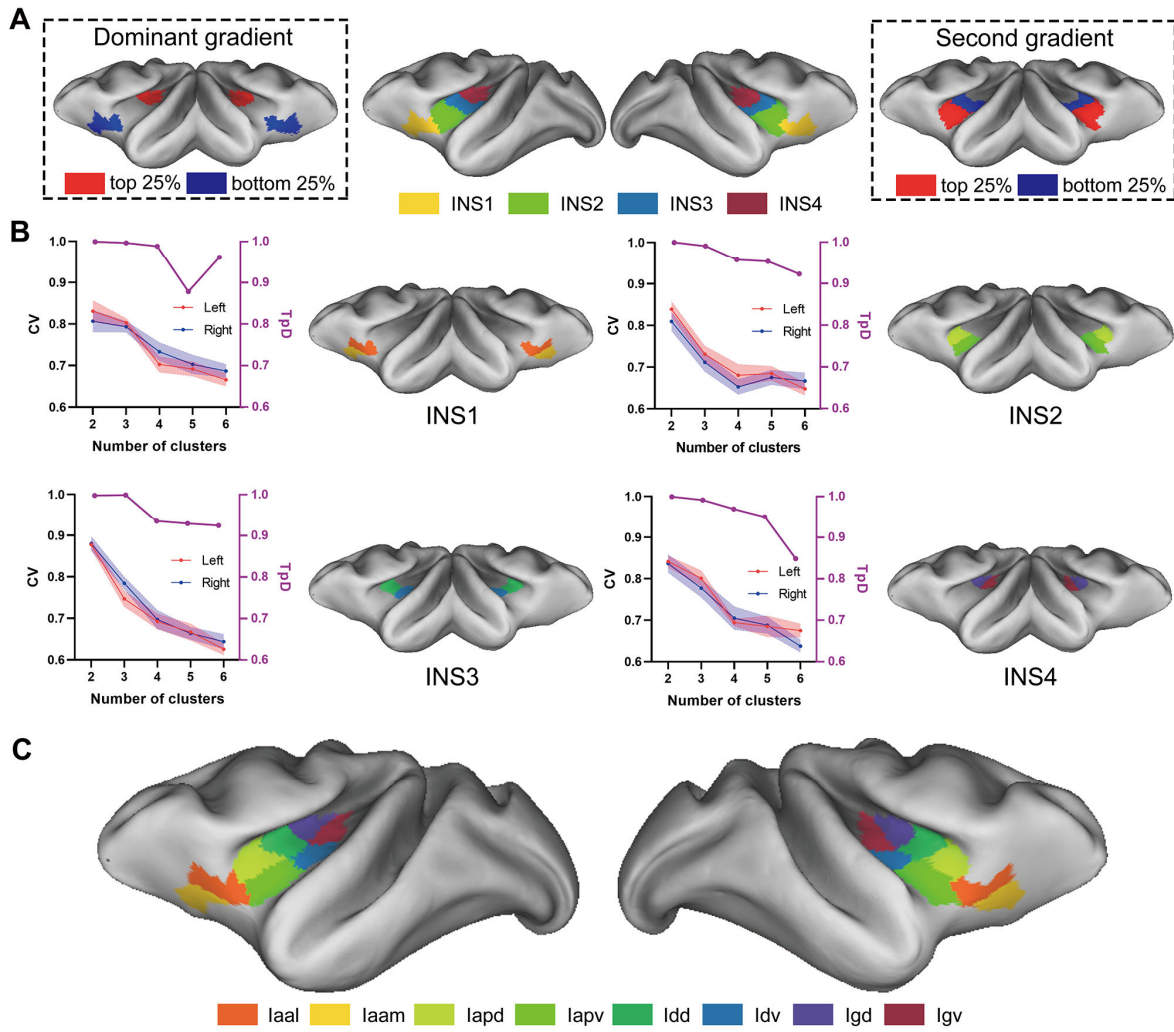
774 and connectivity-based subdivisions of all components sequentially. (B) Macaque insula

775 cytoarchitecture gradients were obtained from Gallay et al.'s study (Gallay et al. 2012b). (C)

776 The insula cytoarchitecture of Paxinos et al.'s (Paxinos et al. 2009) and Calabrese et al.'s

777 (Calabrese et al. 2015b) macaque atlas was mapped to the F99 surface space. (D) Macaque

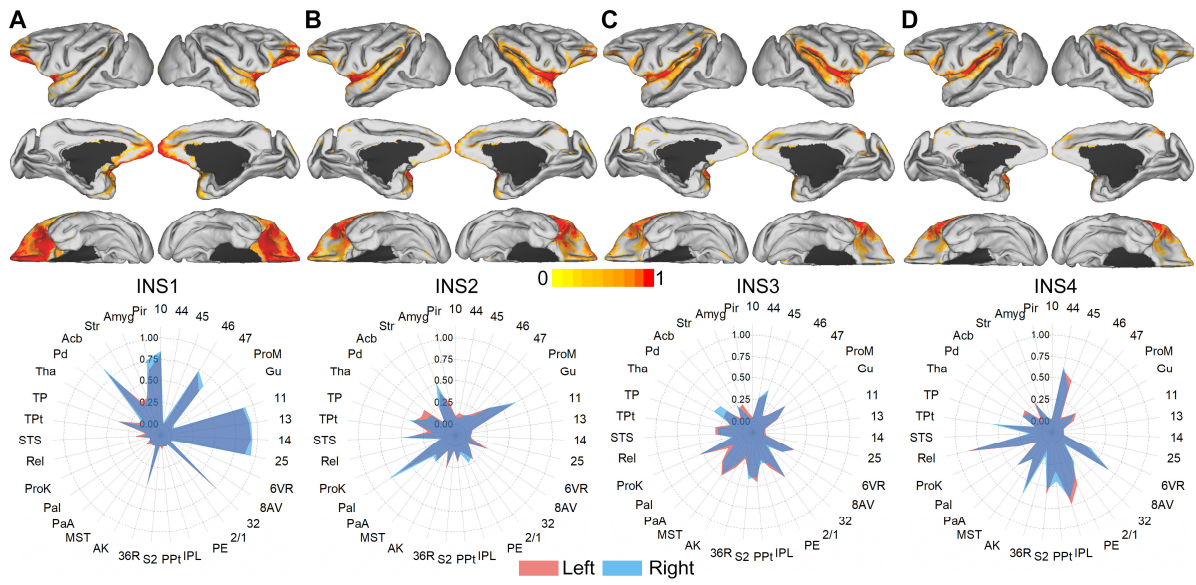778 insula cytoarchitecture was obtained from Evrard et al.'s study (Evrard et al. 2014)
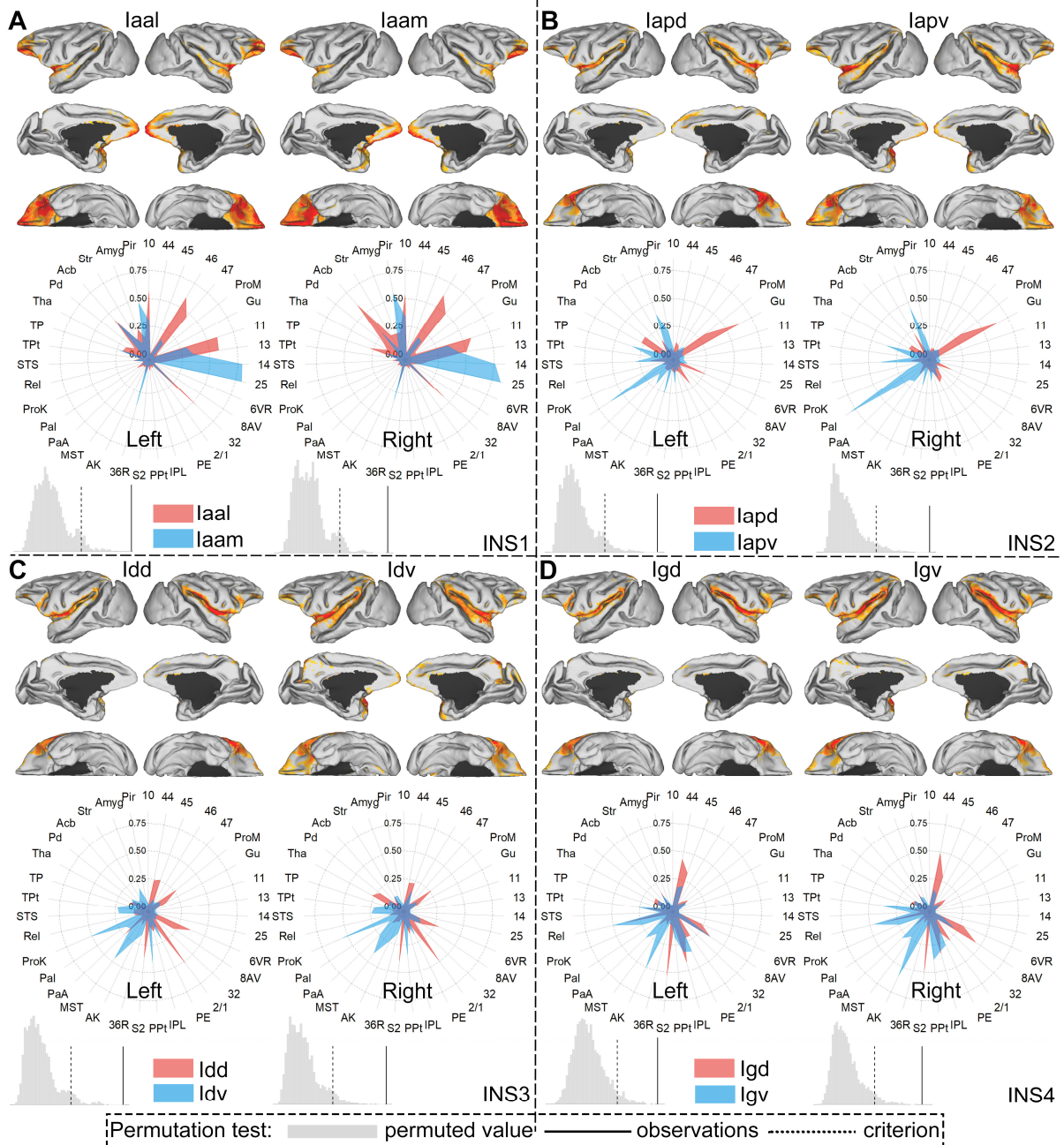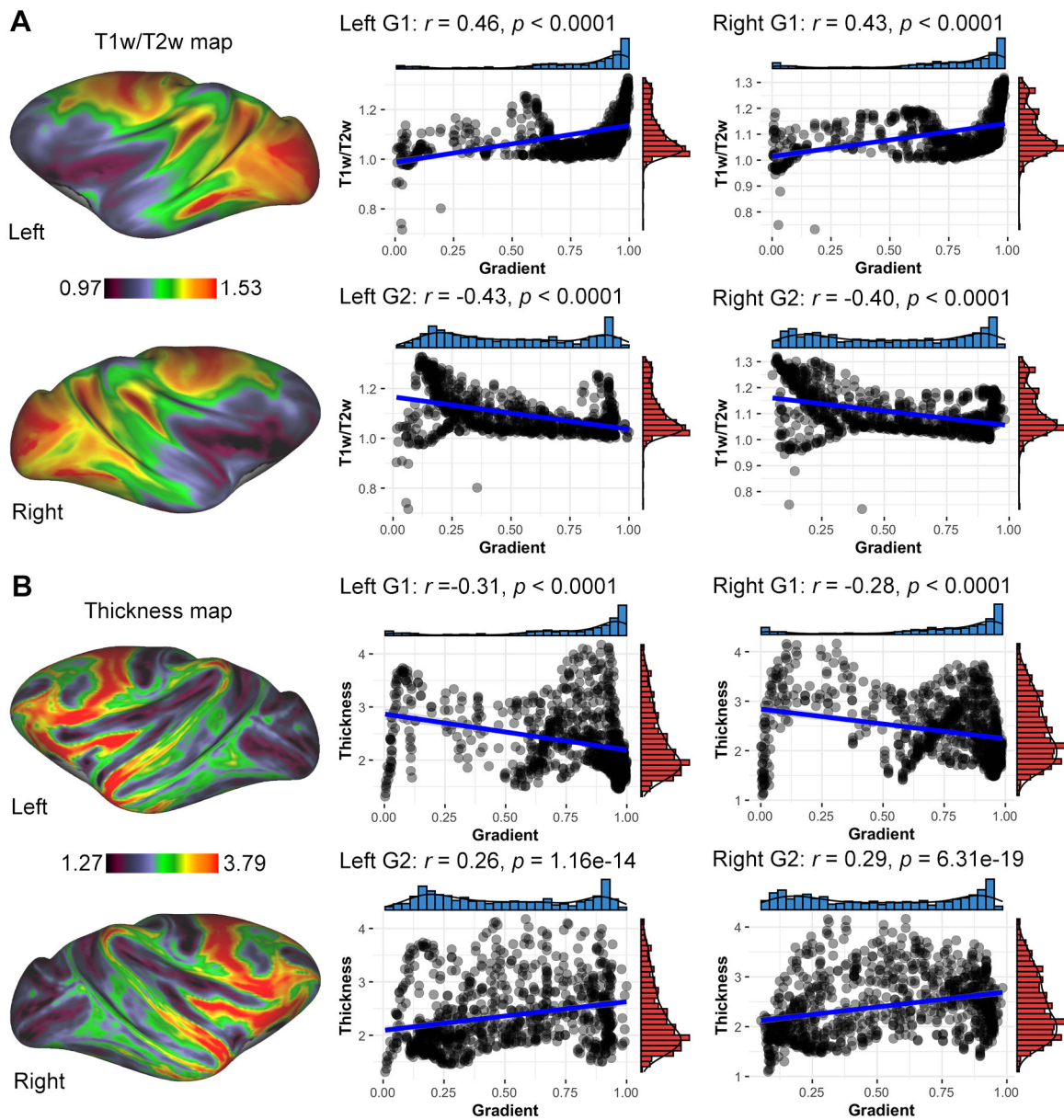
779 **Figure 1**

781 **Figure 2**

782

Figure 3

Figure 4

787 **Figure 5**

788

789 **Figure 6**

790